remote sensing

MDPI

Article

Drop Size Distribution Variability in Central Argentina during RELAMPAGO-CACTI

Candela Casanovas [1,2,3,*], Paola Salio [1,2,3], Victoria Galligani [2,3,4], Brenda Dolan [5] and Stephen W. Nesbitt [6]

1 Departamento de Ciencias de la Atmósfera y los Océanos, Facultad de Ciencias Exactas y Naturales, Universidad de Buenos Aires, Buenos Aires 1428, Argentina; salio@cima.fcen.uba.ar
2 CONICET—Universidad de Buenos Aires, Centro de Investigaciones del Mar y la Atmósfera (CIMA), Buenos Aires 1428, Argentina; victoria.galligani@cima.fcen.uba.ar
3 CNRS—IRD—CONICET—UBA, Instituto Franco-Argentino para el Estudio del Clima y sus Impactos (IRL 3351 IFAECI), Buenos Aires, 1428, Argentina
4 Facultad de Ciencias Exactas y Naturales, Universidad de Buenos Aires, Buenos Aires 1428, Argentina
5 Department of Atmospheric Science, Colorado State University, Fort Collins, CO 80523, USA; bdolan@colostate.edu
6 Department of Atmospheric Sciences, University of Illinois Urbana-Champaign, Urbana, IL 61801, USA; snesbitt@illinois.edu
* Correspondence: candela.casanovas@cima.fcen.uba.ar

Abstract: The Remote sensing of Electrification, Lightning, And Meso-scale/micro-scale Processes with Adaptive Ground Observations (RELAMPAGO) and the Cloud, Aerosol, and Complex Terrain Interactions Experiment Proposal (CACTI) field campaigns provided an unprecedented thirteen-disdrometer dataset in Central Argentina during the Intensive (IOP, 15 November to 15 December 2018) and Extended (EOP, 15 October 2018 to 30 April 2019) Observational Periods. The drop size distribution (DSD) parameters and their variability were analyzed across the region of interest, which was divided into three subregions characterized by the differing proximity to the Sierras de Córdoba (SDC), in order to assess the impact of complex terrain on the DSD parameters. A rigorous quality control of the data was first performed. The frequency distributions of DSD-derived parameters were analyzed, including the normalized intercept parameter ($\log N_w$), the mean volume diameter (D_0), the mean mass diameter (D_m), the shape parameter (μ), the liquid water content (LWC), and the rain rate (R). The region closest to the SDC presented higher values of $\log N_w$, lower D_0, and higher μ, while the opposite occurred in the farthest region, i.e., the concentration of small drops decreased while the concentration of bigger drops increased with the distance to the east of the SDC. Furthermore, the region closest to the SDC showed a bimodal distribution of D_0: the lower values of D_0 were associated with higher values of $\log N_w$ and were found more frequently during the afternoon, while the higher D_0 were associated with lower $\log N_w$ and occurred more frequently during the night. The data were analyzed in comparison to the statistical analysis of Dolan et al. 2018 and sorted according to the classification proposed in the cited study. The $\log N_w$-D_0 and LWC-D_0 two-dimensional distributions allowed further discussion around the applicability of other mid-latitude and global precipitation classification schemes (startiform/convection) in the region of interest. Finally, three precipitation case studies were analyzed with supporting polarimetric radar data in order to relate the DSD characteristics to the precipitation type and the microphysical processes involved in each case.

Keywords: DSD; drop size distribution; precipitation; complex terrain

Citation: Casanovas, C.; Salio, P.; Galligani, V.; Dolan, B.; Nesbitt, S.W. Drop Size Distribution Variability in Central Argentina during RELAMPAGO-CACTI. *Remote Sens.* **2021**, *13*, 2026. https://doi.org/10.3390/rs13112026

Academic Editors: Christopher Kidd and Lisa Milani

Received: 26 April 2021
Accepted: 18 May 2021
Published: 21 May 2021

1. Introduction

The characterization of drop size distributions (DSDs) is fundamental for both the remote sensing of precipitation and its representation in numerical models. It is directly related to the radar reflectivity (Z) and the rain rate (R), which makes it an essential parameter for quantitative precipitation estimates [1–4]. The parameterizations of microphysical

processes in numerical models also need to assume particle size distributions, generally represented by a gamma distribution with one to three prognostic parameters [5–7], among others.

The DSD varies with the different microphysics and precipitation regimes across the world [8]. The classification of convective/stratiform precipitation from DSD parameters has been the subject of many studies, and different classification schemes have been proposed, for instance setting thresholds on variables such as the standard deviation of R [9] or establishing separations in the two-parameter space of $\log N_w$-D_0, related to the number concentration and mean size of drops, respectively [10,11] (BR09, TH15). Recently, Ref. [12] (D18) applied principal component analysis (PCA) to a global DSD dataset, revealing the main modes of variability of the DSD in high, mid-, and low latitudes. Based on the PCA analysis, the dataset was divided into six different groups with similar DSD characteristics related to the dominant microphysical processes in each one of them.

Previous works have analyzed DSDs from different regions and climatic regimes and identified the characteristics of continental, maritime, and tropical environments [9–11,13,14]. Distinctive features of orographic DSDs, such as the elevated concentration of small drops compared to the DSDs found in the adjacent plains, were found especially for low to moderate R [15–18]. In addition, several studies have analyzed the DSD in severe weather situations [16] and mesoscale convective systems in various regions of the world [19–21].

Deep moist convection over Southeastern South America (SESA) (blue box in Figure 1a) has awoken interest among the scientific community on a global scale, since it produces extreme storms of great vertical development [22], which are usually associated with high-impact weather [23–25] like giant hail [26], lightning [27,28], intense wind gusts, and, occasionally, tornadoes [29,30]. Mulholland et al. (2018) [31] identified a large number of discrete and multicellular convective events close to Sierras de Córdoba (SDC) (Figure 1b) using ground radar scanning. Most of the extreme convection observed in the area initiates on the high central terrain and the northern tip of the SDC [32]. Due to the environmental conditions, eastward propagation is preferentially observed. The most active months for deep convective storms near the SDC are between November and February or during the transition from austral spring into summer. Discrete convective modes tend to be favored earlier in the austral spring season, whereas multicellular convective modes are skewed toward later in the spring season and into the summer season.

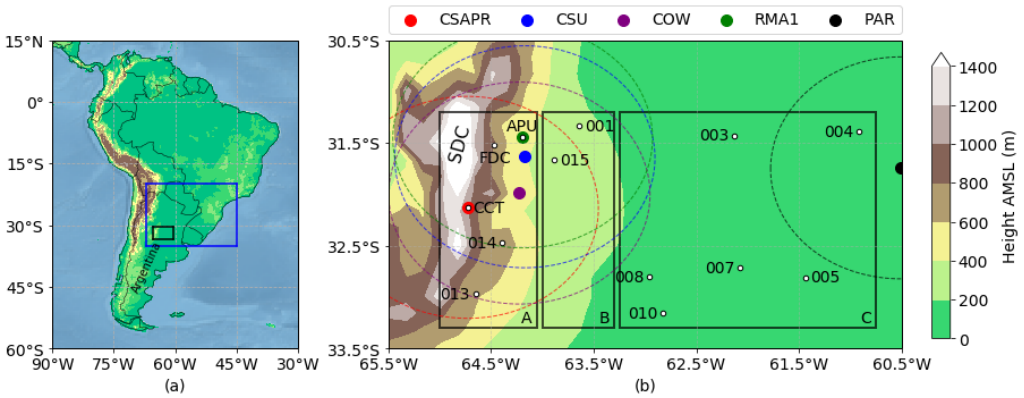

Figure 1. (**a**) Location of the study area in South America indicated by the black box. Southeastern South America (SESA) denoted with a blue box. (**b**) Locations of the thirteen disdrometers analyzed. The shading indicates the height above mean sea level (AMSL) of the Sierras de Córdoba (SDC). The colored markers show the positions of the available radars: the C Scanning ARM Precipitation Radar (CSAPR 2), the Colorado State University C-band Hydrological Instrument for Volumetric Observation (CSU-CHIVO, hereafter CSU), the CSWR C-band on wheels (COW), the Radar Meteorologico Argentino 1 (RMA1), and the Parana C band radar (PAR). The dotted line rings indicate the 120 km range of each radar. The black boxes show the three regions into which the study area was subdivided.

The field campaigns Remote sensing of Electrification, Lightning, And Meso-scale/micro-scale Processes with Adaptive Ground Observations (RELAMPAGO) [33] and the Cloud, Aerosol and Complex Terrain Interactions Experiment Proposal (CACTI) [34] took place between 15 October 2018 and 30 April 2019, leeward of the Andes Mountains in Central Argentina (http://relampago-cacti.org (accessed on 1 October 2019)). RELAMPAGO consisted of intensive operations between 1 November and 16 December 2018 and an extended period of hydro-meteorological observations between May 2018 and May 2019. CACTI studied the atmospheric boundary layer, aerosols, and clouds in a fixed location in Yacanto de Calamuchita, next to the highest peaks of the SDC, between October 2018 and April 2019. Both experiments have built a unique and unprecedented dataset in the region. In the context of the RELAMPAGO-CACTI field campaigns, the present study compiled a dataset including thirteen disdrometers in different locations of Central Argentina, covering over seven months of data.

The main objective of this study was to present a robust characterization of the DSD and its variability in Central Argentina, making use of the exceptional amount of data that was gathered during RELAMPAGO-CACTI field campaigns, and makes a contribution to the understanding of physical precipitation processes during the warm season in the mid-latitudes.

Section 2 includes a description of the dataset and the methodologies for the quality control and the estimation of the DSD parameters. In Section 3.1, the distribution of the different DSD parameters is analyzed as a function of the distance to the SDC, and the data are sorted according to the D18 classification. Section 3.2 presents three case studies, which, with supporting polarimetric radar data, relate the DSD characteristics described in the previous section with the precipitation regime and microphysics involved. Finally, Section 4 presents the summary and conclusions of the study.

2. Materials and Methods

The DSD sample compiles thirteen OTT Parsivel disdrometer datasets from Central Argentina. Twelve disdrometers were installed during RELAMPAGO-CACTI, with the support of the National Science Foundation (NSF), NASA Global Precipitation Measurement-Ground Validation (GPM-GV), and the Department of Energy of the United States (DOE), and one belongs to the Sistema Nacional de Radares Meteorológicos (SINARAME). The RELAMPAGO data were downloaded from the Earth Observing Laboratory (EOL-NCAR) website (https://www.eol.ucar.edu (accessed on 1 October 2019)); the CACTI data were downloaded from the Atmospheric Radiation Measurement program (ARM-DOE) website (https://adc.arm.gov/discovery (accessed on 1 October 2019)); the GPM disdrometer data were provided by the Global Precipitation Measurement Ground Validation Office (https://trmm-fc.gsfc.nasa.gov/ftp/pub/tokay/relampago/ (accessed on 1 October 2019)); and the SINARAME data were available under a cooperation agreement between the Secretaría de Infraestructura y Política Hídrica de la Nación and the Facultad de Ciencias Exactas y Naturales, Universidad de Buenos Aires. The thirteen disdrometers were located between 31.3°S and 33.2°S and between 60.9°W and 64.7°W, as shown in Figure 1b, which also shows the three proposed regions in which the study area was subdivided in order to analyze the impact of complex terrain and the proximity to the SDC on the DSD parameters. Table 1 details information about the sites, project, location, height above mean sea level (AMSL), time frame, sampling time, time between samples, and the length of each dataset.

Table 1. Details of each disdrometer dataset including project, type of disdrometer, location, height AMSL, period of observation, sampling time, time between observations, total number of observations and region (* valid 1 min samples that remain after the QC and filters applied to the dataset).

Id.	Project	Disdrometer	Latitude (°)	Longitude (°)	Height AMSL (m)	Starting Date	Ending Date	Sampling Time (min)	Time between Samples (min)	No. of Observations *	Region
001	NSF-RELAMPAGO	OTT Parsivel 2	−31.331	−63.641	253	25-05-2018	12-03-2019	1	1	3905	B
003	NSF-RELAMPAGO	OTT Parsivel 2	−31.428	−62.133	111	16-07-2018	03-05-2019	1	1	5647	C
004	NSF-RELAMPAGO	OTT Parsivel 2	−31.392	−60.911	25	25-07-2018	04-05-2019	1	1	7186	C
005	NSF-RELAMPAGO	OTT Parsivel 2	−32.806	−61.435	96	26-05-2018	08-05-2019	1	1	7458	C
007	NSF-RELAMPAGO	OTT Parsivel 2	−32.716	−62.075	112	25-05-2018	09-05-2019	1	1	6705	C
008	NSF-RELAMPAGO	OTT Parsivel 2	−32.804	−62.960	147	22-05-2018	28-03-2019	1	1	4423	C
010	NSF-RELAMPAGO	OTT Parsivel 2	−33.156	−62.823	121	25-05-2018	20-03-2019	1	1	4692	C
013	NSF-RELAMPAGO	OTT Parsivel 2	−32.967	−64.652	1111	29-05-2018	13-03-2019	1	1	7500	A
014	NSF-RELAMPAGO	OTT Parsivel 2	−32.472	−64.395	631	26-05-2018	05-05-2019	1	1	7938	A
015	NSF-RELAMPAGO	OTT Parsivel 2	−31.668	−63.882	334	25-05-2018	11-03-2019	1	1	4711	B
APU	NASA-GPM	OTT Parsivel 2	−31.438	−64.194	432	06-12-2018	09-02-2019	1	1	2210	A
CCT	DOE-CACTI	OTT Parsivel 2	−32.126	−64.728	1142	01-10-2018	27-04-2019	1	1	9720	A
FDC	SINARAME	OTT Parsivel 1	−31.521	−64.465	705	06-01-2019	31-05-2019	1	10	300	A

During the field experiment, five C-band radars were available: CSAPR (DOE-CACTI), CSU (NSF-RELAMPAGO), COW (NSF-RELAMPAGO), RMA1 (SINARAME), and PAR (Instituto Nacional de Tecnología Agropecuaria (INTA)). Their locations and 120 km range are shown in Figure 1. However, only CSU and PAR were used in the present study, as a visual aid in case studies to assist with event description. For further details about the radar capabilities, see Nesbitt et al. 2021 [33].

The OTT Parsivel disdrometer [35–37] is an optical sensor that measures the attenuation generated by the precipitation particles that go through a laser beam during a sampling time, which is usually one minute. The amplitude of the attenuation is related to the particle size, and the length of the signal is related to its fall speed; therefore, the raw data provided by the disdrometer are a two-dimensional histogram of drop sizes D_i ($i = 1, \ldots, 32$) and fall speeds V_j ($j = 1, \ldots, 32$). Then, the DSD can be computed summing over j.

Before calculating the DSD, a quality control was performed on the data. First, it was necessary to filter out possible solid precipitation particles, non-meteorological signals such as spiders, spider webs, or insects, and errors related to border effects, such as drops that were captured only partially and were therefore classified as smaller drops with anomalously high fall speeds, or the opposite case where two or more drops fall through the sampling area simultaneously and were therefore classified as a single bigger drop with an anomalously low fall speed [16,38]. This was achieved following the methodology used in many previous studies [15,39–42], which consisted of removing the drops whose measured fall speed V_j differed by more than 50% from the expected terminal velocity for a drop of its size, given by the following expression, which is a polynomial fit to the experimental results obtained by Gunn and Kinzer (1949) [43]:

$$v_D = -0.193 + 4.96D - 0.904D^2 + 0.0566D^3 \quad (1)$$

Equation (1) was developed considering sea level pressure conditions. Foote and Du Toit (1969) [44] showed that, between 1013 and 900 mb, terminal raindrop fall speeds do not change significantly due to air density effects, and all disdrometers are located approximately within that pressure range. That is why air density effects were not considered.

Figure 2 shows the normalized frequency of each diameter (D_i) and fall speed (V_j) for the whole-sample thirteen-disdrometer dataset before quality control. The gray curve represents the expected terminal velocity given by Equation (1), and the shaded area indicates the ±50% thresholds.

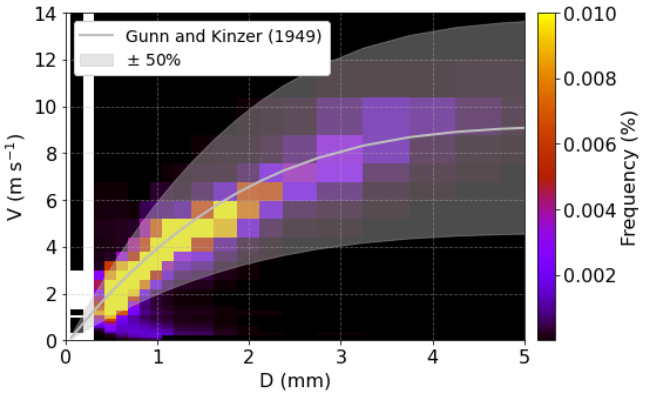

Figure 2. Normalized histogram of measured fall speed vs. drop size for the entire 13-disdrometer dataset before quality control. Zero values are masked (white). The gray curve represents the expected terminal velocity given by Equation (1), and the shaded area indicates the ±50% thresholds.

Although the maximum frequencies fell mostly inside the shaded area, the unfiltered sample presented above-zero frequencies for almost all sizes and speeds in the spectrum (zero values were masked), which proved the importance of this step. The largest portion

of the drops removed presented diameters between 0.3 mm and 1.6 mm and fall speeds lower than half the terminal velocity expected for raindrops of those sizes, and they were non-precipitation particles, small drizzle particles that may be affected by turbulence, or particles that go through the sampling area almost horizontally due to strong winds.

Following D18 and TH15, only 1 min DSD data with at least 100 total drops and R > 0.05 mm h^{-1} during at least 3 consecutive minutes (except for FDC, which has 1 observation every 10 min) were analyzed. This prevented a large number of very small samples from skewing the analysis towards an underestimation of the DSD parameters [45,46]. This step removed 56% of the data points, but only 6% of the total rainfall.

The 1 min DSD was then computed from the raw data according to the following expression:

$$N(D_i) = \frac{1}{S_{eff}(D_i) \times t \times \Delta D_i} \sum_{j=1}^{32} \frac{n_{ij}}{v_{D_i}} \tag{2}$$

where $S_{eff}(D_i)$ is the effective sampling area (m^2), t is the sampling time (60 s in our dataset), ΔD_i is the bin width (mm), n_{ij} is the number of drops of size D_i and fall speed V_j, and v_{D_i} (m s^{-1}) is the terminal velocity given by Equation (1). The units of $N(D)$ are mm^{-1} m^{-3}, so that multiplying by ΔD_i (mm) yields the number of drops of size between $D_i - \frac{1}{2}\Delta D_i$ and $D_i + \frac{1}{2}\Delta D_i$ per cubic meter. $S_{eff}(D_i) = L\left(W - \frac{D_i}{2}\right)$ accounts for the border effects previously mentioned, where L = 180 mm and W = 30 mm were the length and width of the laser beam, respectively. v_{D_i} was used instead of the measured fall speed V_j because the Parsivel disdrometer underestimated the speed of drops, particularly for the smaller diameters, around 1.1 mm [37], and this could have a significant effect on the estimated DSD and its parameters.

The liquid water content (LWC) can be obtained by integrating $N(D)$ as follows:

$$LWC = \frac{\pi \rho_w}{6} \sum_{i=1}^{32} D_i^3 N(D_i) \Delta D_i, \tag{3}$$

where ρ_w is the water density (g mm^{-3}). R is also computed integrating $N(D)$:

$$R = 6\pi 10^{-4} \sum_{i=1}^{32} D_i^3 v_{D_i} N(D_i) \Delta D_i. \tag{4}$$

The four-parameter modified gamma distribution is often used to represent size distributions [47] of cloud drops and precipitation particles, both liquid and solid. The exponential distribution [48], the power law [49], and the normalized gamma with three free parameters [50] are special cases of the former. The last one is often the best fit for rain DSDs [51,52] and is a function of the normalized intercept parameter N_w (mm^{-1} m^{-3}), the mean mass diameter D_m (mm), and the shape parameter μ following:

$$N(D) = N_w f(\mu) \left(\frac{D}{D_m}\right)^{\mu} exp\left[-(4+\mu)\frac{D}{D_m}\right], \tag{5}$$

where $f(\mu)$ contains the gamma function:

$$f(\mu) = \frac{6}{4^4} \frac{(4+\mu)^{\mu+4}}{\Gamma(\mu+4)}. \tag{6}$$

D_m is the first moment of the mass spectrum $m(D) = \frac{\pi \rho_w}{6 \times 10^3} N(D) D^3$ and can be written as the ratio between the fourth and third moment of $N(D)$:

$$D_m = \frac{E[D^4]}{E[D^3]} = \frac{\int D^4 N(D) dD}{\int D^3 N(D) dD}, \tag{7}$$

and N_w is the intercept parameter of an exponential function ($\mu = 0$) with the same LWC:

$$N_w = \frac{4^4}{\pi \rho_w} \left(\frac{LWC}{D_m^4} \right). \tag{8}$$

The normalized gamma distribution can also be expressed in terms of the mean volume diameter D_0, which is the diameter that accumulates half LWC:

$$\frac{\pi}{6} \rho_w \int_0^{D_0} D^3 N(D) dD = \frac{1}{2} LWC, \tag{9}$$

and is related to D_m and N_w through the following equations:

$$D_m = \frac{4 + \mu}{3.67 + \mu} D_0, \tag{10}$$

$$N_w = \frac{3.67^4 10^3 LWC}{\pi \rho_w D_0^4}. \tag{11}$$

The shape parameter μ was obtained by minimizing the mean-squared error between the measured DSD and the normalized gamma function defined by the estimated N_w and D_m, with μ varying between -10 and 20. The gamma fit and associated parameters were calculated using the library PyDSD (https://github.com/josephhardinee/PyDSD (accessed on 1 October 2019)) [53].

The normalized gamma fit was used here in order to compare our results with the large number of previous studies that also take this approach, although it may not fully capture the true spectrum of DSDs [54]. The gamma fitted DSDs were further restricted to only those with μ values in the range from -4 to 15, to ensure the gamma fit was a reasonable assumption, following D18. This condition removed 39% of observations (after the filtering described earlier) and 7% of the total rainfall, and the proportion increased with the proximity to the SDC. The removed samples presented much lower values of D_m and R than the remaining samples, which might indicate drizzle or very small drops going through the sampling area repeatedly because of turbulent motion [55]. These conditions generated a database of 72,395 raining minutes representative of a Southern Hemisphere warm season in mid latitudes.

3. Results

3.1. Characterization of the DSD during RELAMPAGO-CACTI

In order to evaluate how the proximity to the complex terrain in the SDC affects the DSD parameters, the study area was subdivided into three regions, as shown in Figure 1b: Region A is the closest to the SDC and includes the disdrometers APU, FDC, CCT, 014, and 015, all located above 400 m AMSL; Region B includes disdrometers 001 and 015, both between 200 m and 400 m AMSL; and Region C includes disdrometers 003, 004, 005, 007, 008, and 010, all of them below 200 m AMSL and well within the plains, approximately 350 km from the SDC. It is worth mentioning that Region B had only 8616 data points, while Regions A and B had 27,668 and 36,111, respectively, so this should be taken into consideration in the following analysis.

Figure 3 shows the violin plots of different DSD parameters for each region. The dashed lines indicate the median, and the dotted lines indicate the first and third quartiles (P25 and P75, respectively). The data were normalized so that each violin had the same area, which made it easier to compare samples of different sizes. Additionally, Table 2 lists the mean value, mode, standard deviation, minimum, maximum, and fifth (P05) and ninety-fifth percentiles (P95) for each DSD parameter at each region.

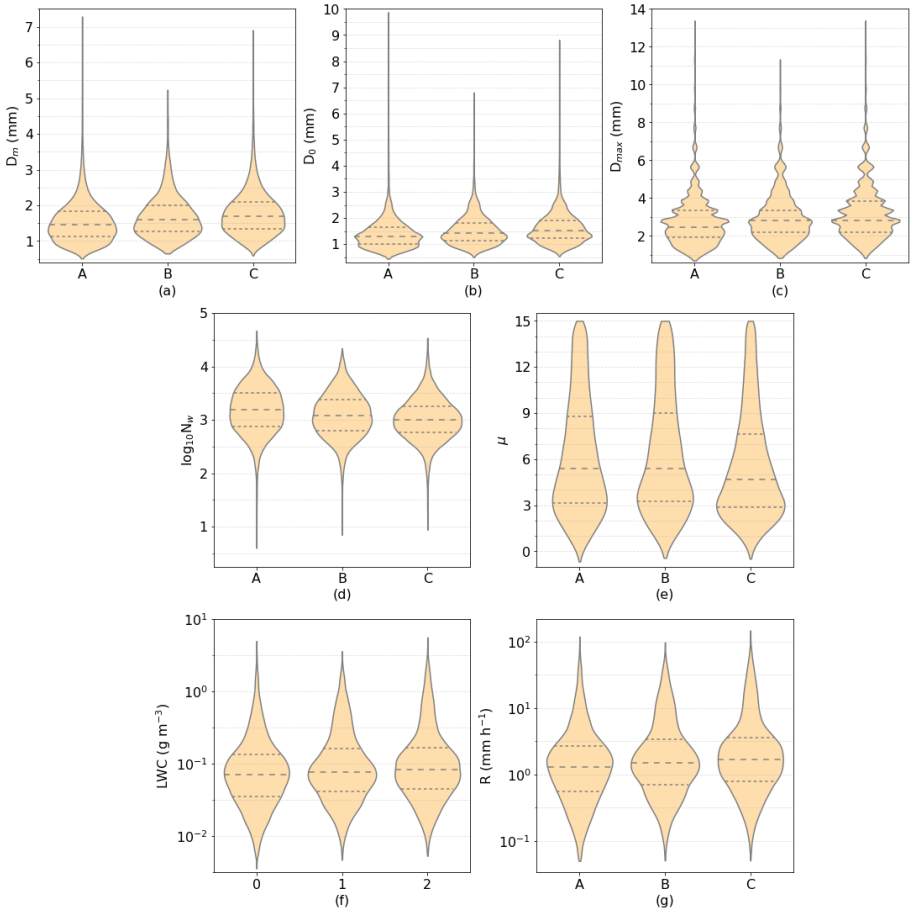

Figure 3. Violin plots of: (**a**) D_m, (**b**) D_0, (**c**) D_{max}, (**d**) logN_w, (**e**) μ, (**f**) LWC, and (**g**) R for the three study regions. The dashed line indicates the median, and the dotted lines indicate the first (P25) and third (P75) quartiles. The data were normalized so that each violin has the same area.

Table 2. Statistics (mean, mode, standard deviation, min, max, P05, P95) of the different DSD parameters D_m, D_0, D_{max}, logN_w, μ, LWC, and R for each region.

		Mean	Mode	Standard Dev.	Minimum	Maximum	5th Percentile	95th Percentile
D_m	A	1.55	1.30	0.61	0.51	7.29	0.81	2.61
	B	1.69	1.39	0.61	0.65	5.24	0.92	2.86
	C	1.79	1.61	0.65	0.60	6.90	0.97	2.96
D_0	A	1.40	1.29	0.57	0.44	9.88	0.73	2.41
	B	1.54	1.24	0.57	0.50	6.80	0.84	2.60
	C	1.62	1.27	0.60	0.54	8.82	0.88	2.65
D_{max}	A	2.78	2.83	1.29	0.71	13.39	1.22	4.89
	B	3.01	2.83	1.33	0.84	11.33	1.42	5.66
	C	3.21	2.83	1.39	0.84	13.39	1.42	5.66
logN_w	A	3.19	3.07	0.45	0.60	4.67	2.47	3.89
	B	3.09	3.21	0.42	0.85	4.34	2.44	3.77
	C	3.02	2.92	0.40	0.94	4.54	2.41	3.67
μ	A	6.17	2.32	3.76	−0.66	15.00	1.22	13.44
	B	6.30	2.87	3.81	−0.42	15.00	1.37	13.54
	C	5.58	2.47	3.50	−0.48	15.00	1.33	12.84
		Mean	**Mode**	**Standard Dev.**	**Minimum**	**Maximum**	**Percentile 5**	**Percentile 95**
LWC	A	0.14	0.02	0.24	0.00	4.97	0.01	0.49
	B	0.17	0.03	0.27	0.00	3.59	0.02	0.67
	C	0.19	0.03	0.33	0.01	5.57	0.02	0.78
R	A	3.00	0.34	6.17	0.05	119.46	0.17	11.58
	B	3.83	0.38	6.84	0.05	97.99	0.24	16.45
	C	4.44	0.40	8.74	0.05	147.34	0.26	20.03

From Region A to Region C, the median, P25, and P75 of D_m adopted larger values (Figure 3a), as well as the mean and P95 (Table 2). The same happened with D_0 (Figure 3b), which, in addition, presented a bimodal distribution in Region A. The maximum diameter D_{max} was the diameter of the biggest drop in each individual sample, so it was the only parameter that was directly measured by the disdrometer, which classified the drops in size bins of varying width. That is the reason why the violin plots in Figure 3c exhibit irregular borders. In Regions B and C, P25 and the median were higher than in Region A, and in Region C, P75 was higher than in Regions A and B. Moreover, Table 2 shows that the mean of D_{max} grew from A to C. For the three parameters described, Welch's *t*-test (*t*-test for unequal variances and/or unequal sample sizes) indicated that the mean in Region B was larger than in Region A and that the mean in Region C was larger than the mean in Regions A and B, with a 99% confidence level. This means that the probability of finding DSDs with bigger drops increased eastward from SDC.

It should be noted that Welch's *t*-test assumes that the means of different samples from a population are normally distributed, and usually, the sample means are normally distributed for sample sizes above 30, which is why the test is reliable despite the fact that the DSD parameters were not normally distributed.

The median and interquartile range of $\log N_w$ decreased from A to C (Figure 3d), and the mean and P05 and P95 behaved similarly (Table 2). Welch's *t*-test indicated that the mean in A was larger than the mean in B and C and that the mean in B was larger than in C, with a 99% confidence level. Therefore, the parameters analyzed pointed out that the DSDs with higher number concentrations and smaller drops were more frequent near the SDC, and with the growing distance to the east, the number concentrations decreased while the concentration of bigger drops increased. However, Region A presented the broadest range in all four parameters analyzed, which means that although the DSDs with a higher concentration of small drops were more frequent, it was also possible to find DSDs whose characteristics resembled those of Region C.

Regarding μ, there were no noticeable differences between Regions A and B. However, the difference between these two regions and Region C, whose median and interquartile range (Figure 3e), as well as the mean and P95 (Table 2) adopted smaller values, was evident. Welch's *t*-test indicated that the mean in Region A was larger than in Region C and that the mean in Region B was also larger than the mean in Region C, with a 99% confidence level. Smaller μ values were related to broader distributions with higher concentrations of bigger drops, while larger μ values were related to narrower distributions. Hence, the spatial variability of μ was consistent with the behavior of the parameters analyzed previously.

The median and interquartile range of LWC adopted larger values from A to C (Figure 3f). The mean, mode, P05, P95, and maximum value exhibited the same behavior (Table 2). Figure 3g shows the violin plots of R. The median and interquartile range adopted larger values from A to C, and the dispersion also increased. The mean, mode, and P95 showed the same behavior (Table 2). Both for LWC and R, Welch's *t*-test indicated that the mean in Region A was smaller than in Regions B and C and that the mean in Region B was smaller than in Region C, with a 99% confidence level. That is, the probability of finding larger values of LWC and R increased with the distance to the east of the SDC, which was consistent with the increasing concentration of larger drops.

D18 proposed a classification of the DSD based on the principal component analysis (PCA) of a global dataset. The input variables for the PCA analysis were: D_m, $\log N_w$, σ_m (square root of the second moment of the mass spectrum—Equation (8)), logR, logLWC, and $\log N_t$ (total number of drops). First, the data were normalized by subtracting the mean and dividing by the standard deviation, then the covariance matrix was constructed with the input variables, and the orthogonal empirical functions (EOFs) were computed. By setting thresholds (±1.5) on the first two PCs, they defined six groups with independent characteristics. The physical processes in the six groups were explained through supporting radar observations. Group 1 was related to convective precipitation, Group 2 to stratiform

precipitation, Group 3 warm rain showers, Group 4 heavy stratiform precipitation, Group 5 (characteristic of the low-latitudes) robust warm rain processes, and Group 6 (more frequent in the mid-latitudes) ice-based convection, although it may also appear in heavy stratiform rain. Readers are encouraged to read D18 for further details.

The classification shown in Figure 4 was obtained by projecting the data of the present study onto the EOFs derived from the D18 world dataset and applying similar thresholds on the first two PCs. A slightly higher threshold was selected here (±2.3) in order to avoid overlapping between modes. The scatterplots in Figure 4 correspond to the entire dataset (i.e., Regions A, B, and C). The dotted and solid lines show the convective (above)/stratiform (below) separations proposed by BR09 and TH15, respectively. The latter was proposed specifically for oceanic regions of tropical latitudes, so it was not applicable here, and it is shown for reference. Note that the groups resulting from the PCA analysis in D18 were consistent with the BR09 and TH15 separations. Table 3 shows the percentage of observations in each group for the whole dataset and for each region. Sixty-four percent of the data were below the imposed thresholds, falling into the "Ambiguous" category, which means they resembled multiple EOFs. Group 4 had the largest number of observations (18%), and it was followed by Group 6 (9%) associated with mixed-phase storms. The proportion of observations in these two groups increased from Region A to Region C. Six percent of the data were classified as Group 2 with the proportion decreasing eastward of the SDC. Finally, Group 1 was the least frequent, with 4% of the data falling in the category and the proportion increasing eastward of the SDC.

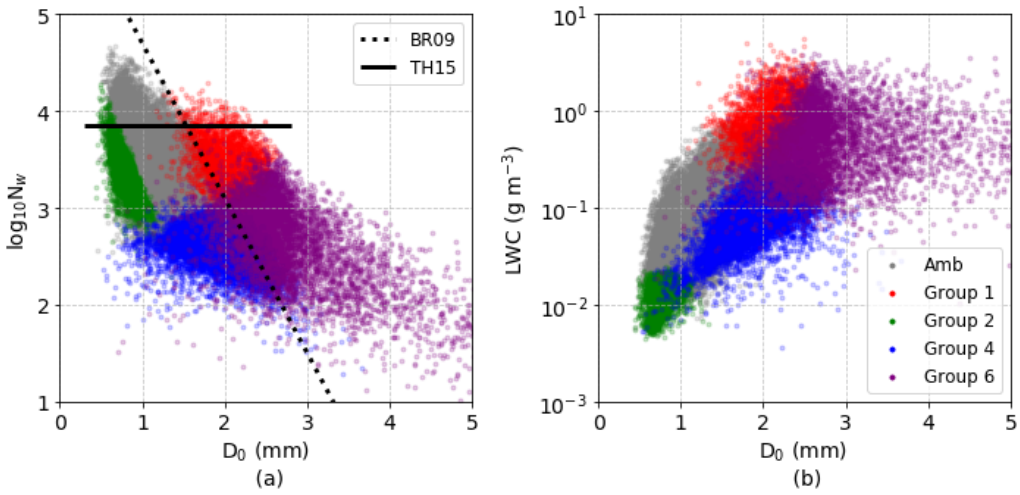

Figure 4. Scatterplots of (**a**) logN_w-D_0 and (**b**) LWC-D_0 for the full dataset (Region A + Region B + Region C). The solid and dotted lines in (**a**) indicate TH15 and BR09 convective/stratiform separations, respectively. The colors indicate the groups of the classification proposed by D18.

Table 3. Percentage of observations in each group of the classification proposed by D18 for all the data and for each region.

	Amb.	Group 1: Convective Precipitation	Group 2: Stratiform Precipitation	Group 3: Weak, Shallow Convection	Group 4: Heavy Stratiform Precipitation	Group 5: Low-Latitude Warm Rain	Group 6: Mixed-Phase Precipitation
ALL	64%	4%	6%	0%	18%	0%	9%
A	70%	3%	8%	0%	13%	0%	6%
B	64%	5%	5%	0%	17%	0%	9%
C	59%	5%	4%	0%	21%	0%	11%

Figure 5a–c shows the 2D histograms of logN_w-D_0 for each region. Region A presented two local maxima: one centered approximately at D_0 = 0.9 mm and logN_w = 3.4 and another one at D_0 = 1.3 mm and logN_w = 3.1. The maximum in Region B was centered at D_0 = 1.3 and logN_w = 3.1, and the maximum in Region C was centered at D_0 = 1.4 mm and logN_w = 3.0. Therefore, from Region A to Region C, the maximum frequencies adopted

smaller values of logN_w and larger D_0, which was consistent with our findings so far. Figure 5 additionally shows that the frequencies in the area of the diagram associated with Group 6 increased from A to C, as well as the frequencies above the dotted line, which were associated with convective DSDs.

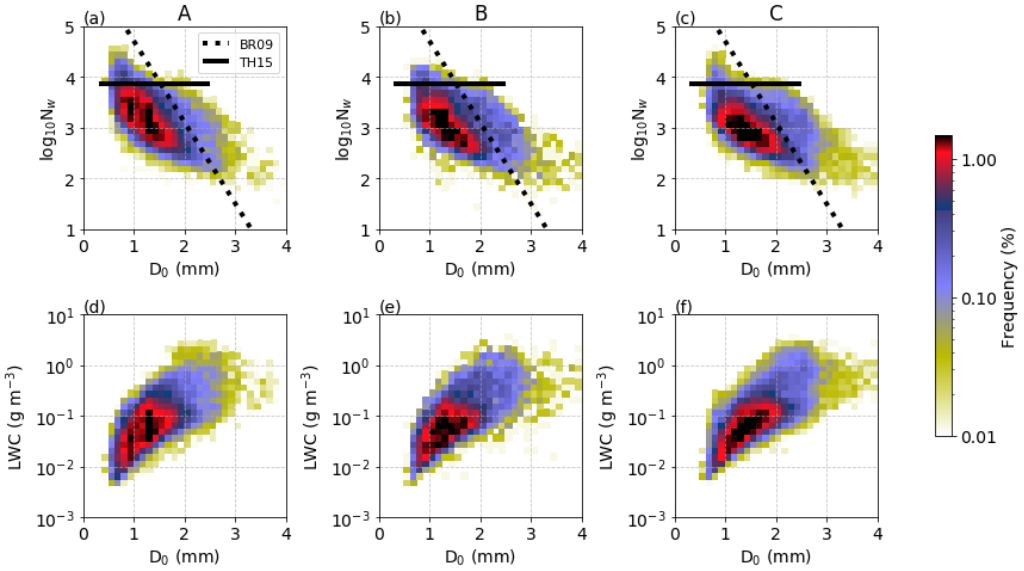

Figure 5. 2D histograms of logN_w-D_0 (**a**–**c**) and LWC-D_0 (**d**–**f**) for Regions A, B, and C. The solid and dotted lines in (**a**–**c**) indicate TH15 and BR09 convective/stratiform separations, respectively.

In the histograms of LWC-D_0 (Figure 5d–f), the shift in the position of the maximum was less apparent. However, there was an increase in the frequency of DSDs with LWC above 0.1 g m^{-3} and D_0 above 2 mm, which was the area of the diagram associated with Group 6. Region A presented again a bimodal distribution, with a local maximum centered approximately at D_0 = 0.9 mm and LWC = 0.03 g m^{-3} and another local maximum centered approximately at D_0 = 1.3 mm and LWC = 0.05 g m^{-3}.

The histograms of D as a function of time (UTC) (Figure 6) show the diurnal cycle of the DSD for Regions A, B, and C separately. The three regions presented a maximum of observations at night (LT is UTC-4hs), which is characteristic of the study region [56–58]. However, the maximum frequencies (above 0.6%) in Region A were centered between 0400 and 0600 UTC; in Region B, the maximum frequencies were centered between 0400 and 0800 UTC; and in Region C, the maximum frequencies were centered between 0600 and 0900 UTC. This might be related to a zonal propagation of the systems.

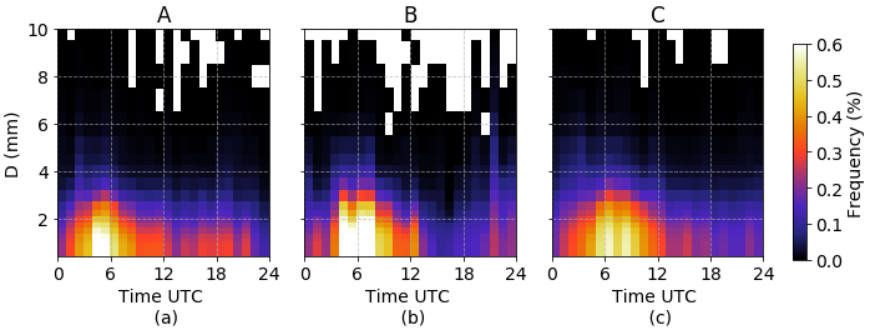

Figure 6. 2D histograms of D (mm) as a function of time (UTC) for Regions A (**a**), B (**b**), and C (**c**). LT is UTC-4hs.

Region A presented a second local maximum in the afternoon, centered approximately at 1800 UTC (i.e., 1400 LT), which was not evident in the other regions. Figure 7 shows the 2D histograms of logN_w-D_0 and LWC-D_0 only for Region A and every three-hour

interval. The night maximum was associated with lower logN_w (maximum centered approximately around three) and larger D_0 (maximum centered approximately around 1.6 mm) (Figure 7b,c), while the afternoon maximum (1500 to 1800 and 1800 to 2100 UTC) was associated with higher logN_w (maximum centered approximately at 3.5) and smaller D_0 values (maximum centered approximately at 1 mm) (Figure 9f,g). LWC did not vary significantly, although from 0300 to 0600 UTC (Figure 9b) and from 1800 to 2100 UTC (Figure 9g), there was a significant increase of DSDs with moderate to large D_0 and large LWC, as well as higher frequencies above the dotted line in the logN_w-D_0 diagrams, which were associated with convection. From 0900 to 1500 UTC and from 2100 to 0300 UTC, the histograms showed a transition between the described regimes.

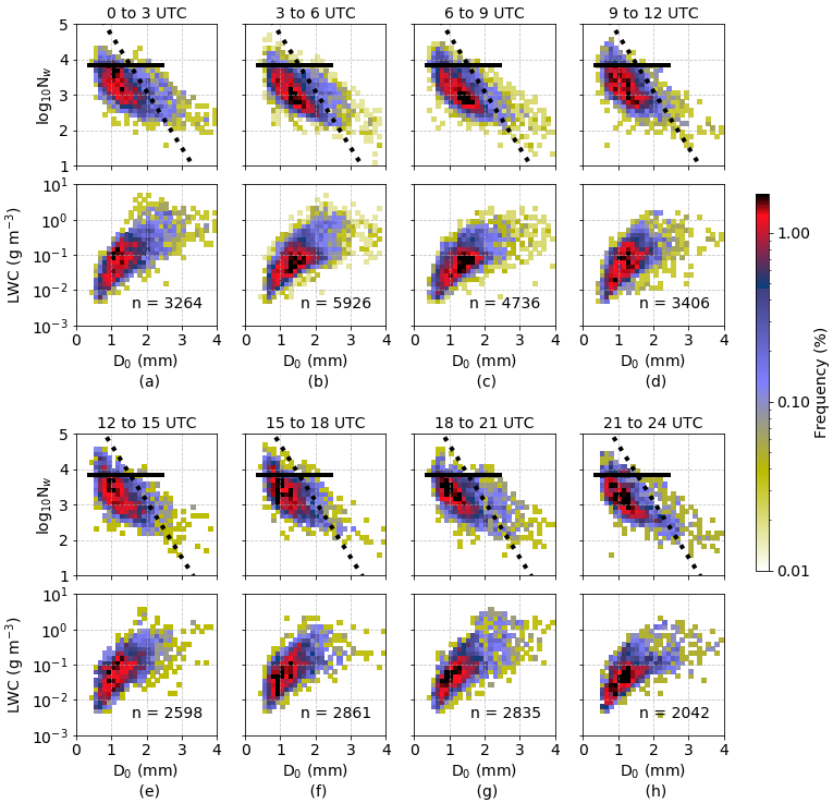

Figure 7. Histograms of logN_w-D_0 and LWC-D_0 for Region A every 3-hour interval: (**a**) 0000 to 0300 UTC, (**b**) 0300 to 0600 UTC, (**c**) 0600 to 0900 UTC, (**d**) 0900 to 1200 UTC, (**e**) 1200 to 1500 UTC, (**f**) 1500 to 1800 UTC, (**g**) 1800 to 2100 UTC, and (**h**) 2100 to 2400 UTC. The solid and dotted lines in the logN_w-D_0 histograms indicate the C/S separations by TH15 and BR09, respectively.

3.2. Case Studies

In this section, we analyzed three case studies with supporting radar data from radars CSU and PAR, relating the DSD characteristics with the type of precipitation and the inferred microphysical processes behind this. The first two cases are examples of the two regimes observed in Region A, and the third case is representative of Region C. The radar data were processed using the PyART library (https://arm-doe.github.io/pyart/ (accessed on 1 October 2019)) [59] and used only as a visual aid to assist with event description.

3.2.1. Case 1: 26 January 2019

This case study was measured by the CCT disdrometer in Region A, which had coincident observations from the CSU radar (see Figure 1b). The sample consisted of 201 consecutive minutes.

At 0200 UTC, a line of convective cells passed over the CCT disdrometer, as shown by the CSU radar (Figure 8g), with maximum reflectivities of around 50 dBZ. The peaks

of R, D_0, and $\log N_w$ at the beginning of the time series in Figure 8a–c mark the passing of the squall line. The low values of μ were consistent with the wide spectrum of sizes (shading in Figure 8a) and high concentration of big drops. The color of the markers indicated the corresponding group following the classification proposed by D18, here obtained after projecting the data onto the D18 world EOFs as described in the previous section. During this initial convective phase, DSDs were classified as Group 1 (convection) and Group 6 (intense ice-based convection). This was consistent with the presence of big drops, which were probably formed by the melting of ice particles. All data points fell in the convective side of BR09 classification (Figure 8e), with moderate to high $\log N_w$ and D_0 and high LWC (Figure 8f).

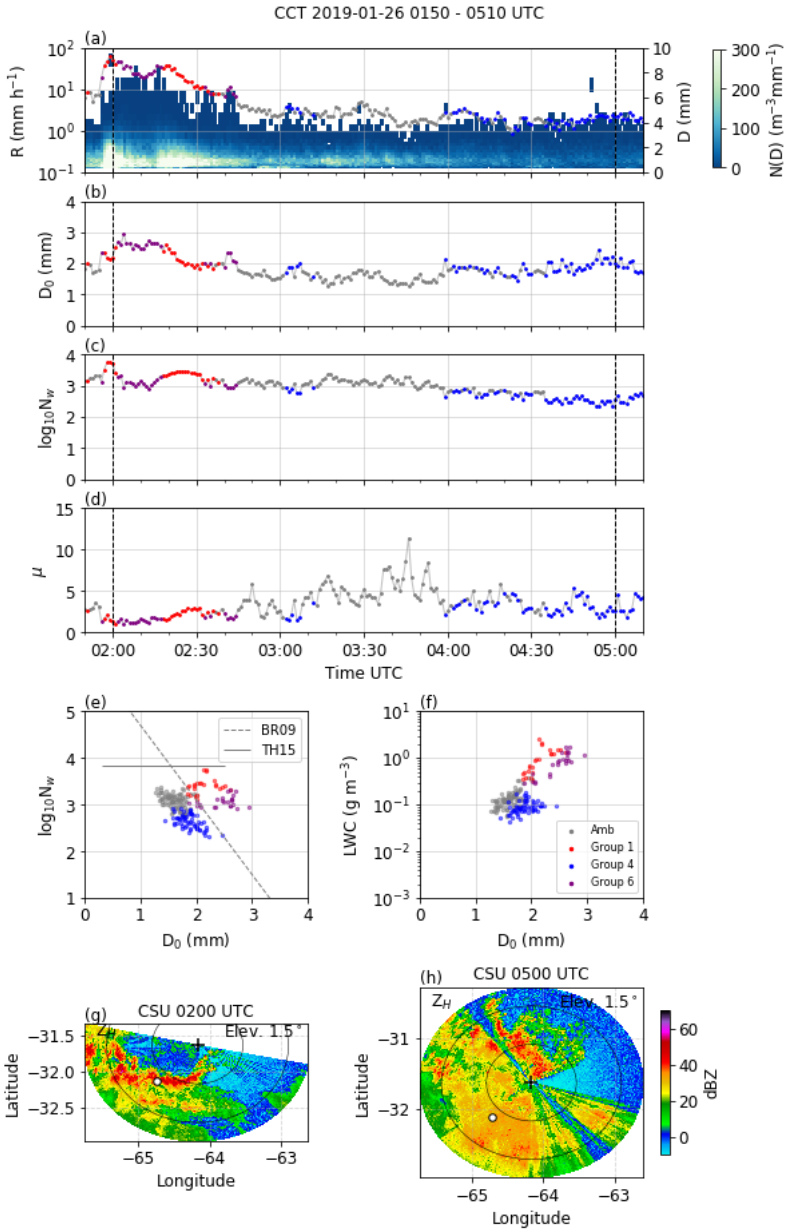

Figure 8. Temporal evolution of (**a**) R (dots) and N(D) (color shading), (**b**) D_0, (**c**) $\log N_w$, and (**d**) μ as measured by disdrometer CCT on January 26, 2019 from 0150 to 0510 UTC. Projection of each 1 min DSD in the (**e**) $\log N_w$-D_0 and (**f**) LWC-D_0 parameter spaces. PPI of Z_H measured by the CSU radar at (**g**) 0200 UTC and (**h**) 0500 UTC. The marker color in (**a**–**f**) indicates the group according to the D18 classification. Dashed lines in (**a**–**d**) mark the times of the radar images. The rings in (**g**,**h**) indicate the 60 and 120 km ranges. The white marker shows the position of the disdrometer.

Following the initial convective phase, a transition phase followed during which μ presented a large variability, logN_w oscillated around three, and D_0 and R decreased. Most DSDs in this phase did not belong to any of the groups proposed by D18 and were classified as "Ambiguous".

Finally, at 0500 UTC, a stratiform system passed over the disdrometer. The PPI in Figure 8h shows a widespread system, with Z_H around 30 dBZover the disdrometer and the bright band signature following approximately the 120 km range, with Z_H over 40 dBZ. As shown in Figure 8a–d, R became stable, and so did N(D); D_0 increased slightly; logN_w decreased slightly; and μ oscillated between approximately two and five, somewhat higher values than those during the convective phase, which was consistent with the narrower size distributions (shading in Figure 8a). Almost all data points during this final stratiform phase were classified as Group 4 (intense stratiform), which was consistent with the moderate values of D_0 and logN_w and the strong bright band signature. The BR09 separation line also classified this phase as stratiform (Figure 8e), and LWC was significantly lower than in the previous convective phase (Figure 8f), which was consistent with the lower values of logN_w and D_0.

Both D18 and BR09 classifications were successful in this case study, with the initial convective phase well classified as convective and the final stratiform phase well classified as stratiform in both cases. Clearly, TH15 classification did not apply in this case and would not be applicable in the following cases either, since, as was mentioned before, it was specifically developed for the oceanic regions of tropical latitudes. It is included however in all the logN_w-D_0 diagrams for visual reference.

3.2.2. Case 2: 17 January 2019

Case 2 was a case of weak, shallow, and unorganized convection in Region A, measured by CCT with coincident observations from the CSU radar. The sample consisted of 337 consecutive minutes.

Figure 9g,h shows a number of isolated convective cells, with reflectivities no higher than 30–35 dBZ, as observed by the CSU radar. The time series in Figure 9a–d show great variability, consistent with the successive passing of convective cells over the disdrometer. The size spectrum of drops (shading in Figure 9a) was much narrower than in the previous case; D_0 was significantly smaller, oscillating between 1 and 2 mm, and logN_w was significantly higher, oscillating between three and four.

Most data points were classified as ambiguous according to the D18 classification applied to the present database. Only a few were classified as Group 2 (stratiform) and Group 4 (intense stratiform). In the logN_w-D_0 space, all data points fell in the stratiform area of the BR09 separation (Figure 9e). Neither classification worked in this case. However, the characteristics of the event were compatible to those of Group 3 in the D18 classification, associated with weak echoes and shallow convection. It is possible that the method failed in this case because of the underrepresentation of subtropical latitudes and mountainous regions in the D18 world dataset, as well as the fact that all locations in that dataset belonged to the Northern Hemisphere. It is also possible that there were additional modes of variability of the DSD that were better explained by higher order EOFs and therefore were not described by the proposed classification (D18).

The cases analyzed so far were examples of the two regimes identified in Region A: Case 1, which took place at night, was characterized by lower N_w and larger D_0, while Case 2, which took place during the afternoon, presented significantly higher values of N_w and much smaller D_0.

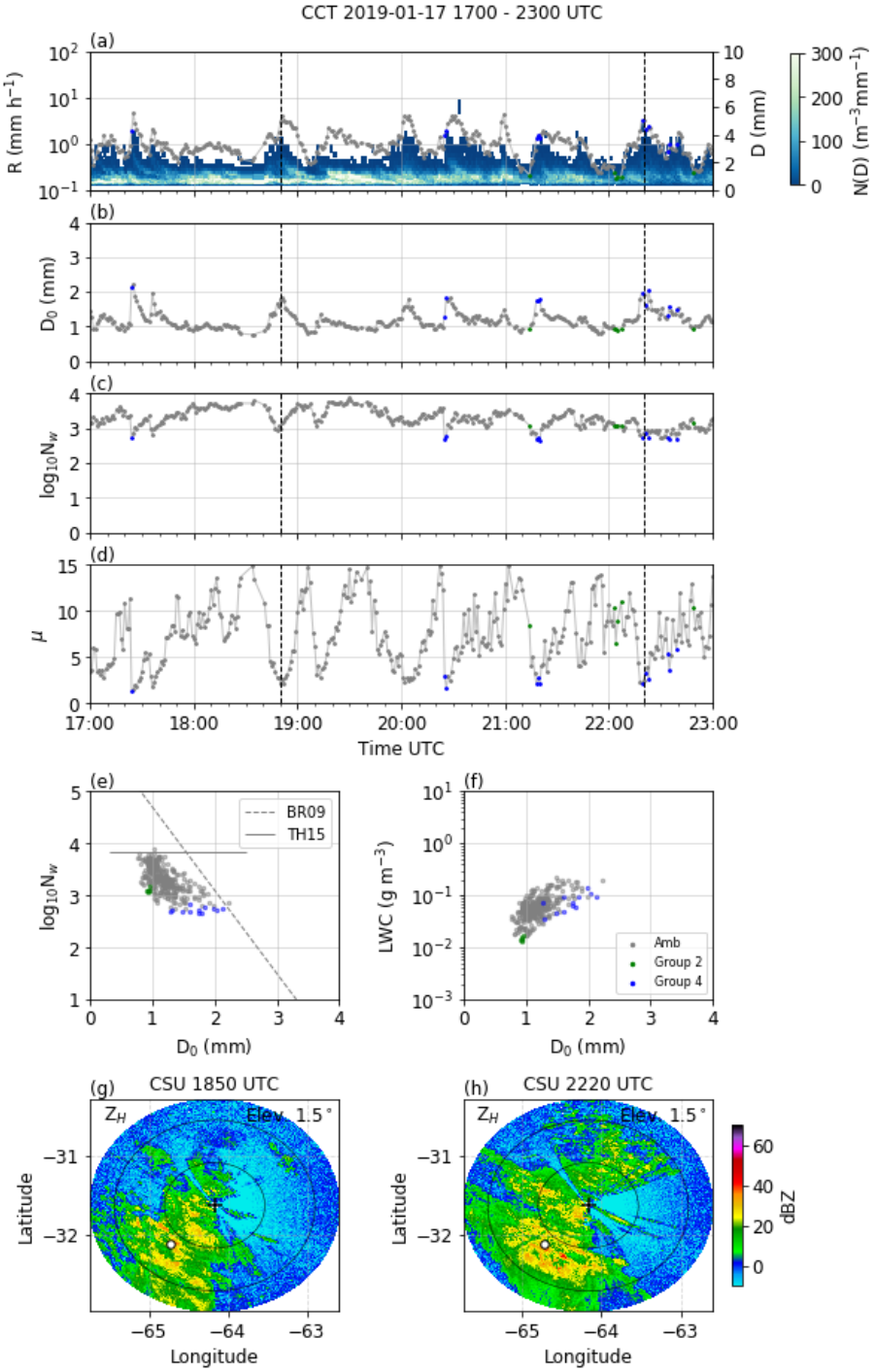

Figure 9. Temporal evolution of (**a**) R (dots) and $N(D)$ (color shading), (**b**) D_0, (**c**) $\log N_w$, and (**d**) μ as measured by disdrometer CCT on 17 January 2019 from 1700 to 2300 UTC. Projection of each 1 min DSD in the (**e**) $\log N_w$-D_0 and (**f**) LWC-D_0 parameter spaces. PPI of Z_H measured by the CSU radar at (**g**) 1850 UTC and (**h**) 2220 UTC. The marker color in (**a**–**f**) indicates the group according to the D18 classification. Dashed lines in (**a**–**d**) mark the times of the radar images. The rings in (**g**,**h**) indicate the 60 and 120 km ranges. The white marker shows the position of the disdrometer.

3.2.3. Case 3: 4 March 2019

Case 3 was similar to Case 1 in that both consisted of an initial convective phase and a final stratiform phase. It was measured by disdrometer 005, which was within the 240 km range of the PAR radar (Figure 1b). The sample consisted of 449 consecutive minutes.

The initial convective phase in Case 3 extended from the beginning of the time series up to approximately 0500 UTC (Figure 10), with elevated R, D_0 around 3 mm, logN_w around 3, and low μ values, consistent with the wide spectrum of sizes (shading in Figure 10a). The PPI taken by the PAR radar at 0330 UTC (Figure 10g) showed an intense squall line, with maximum reflectivities around 50 dBZ. Most data points of the initial phase were classified as Group 6 (intense ice-based convection) in the D18 classification and some as Group 1 (convection), and all of them fell in the convective area of the BR09 separation (Figure 10e), with the highest LWC of the time series (Figure 10f).

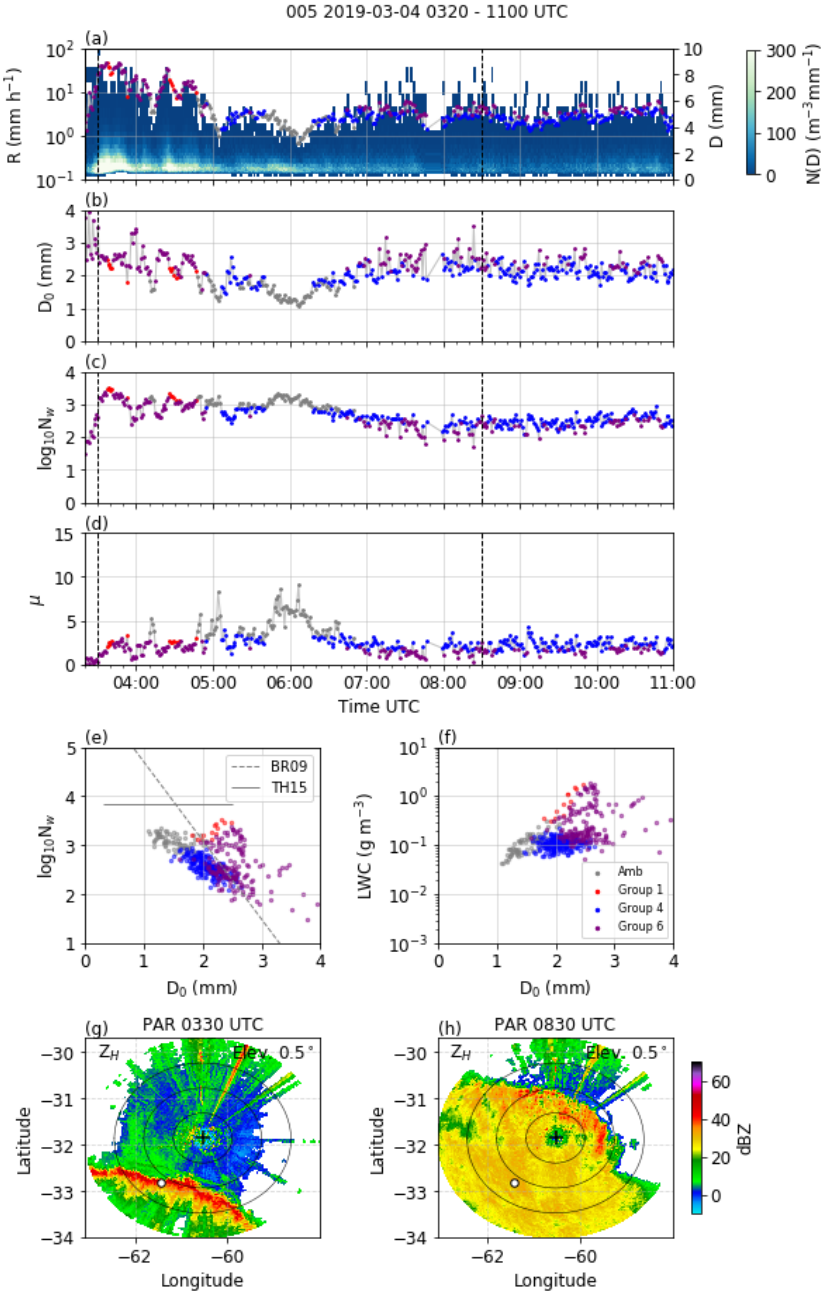

Figure 10. Temporal evolution of (**a**) R (dots) and N(D) (color shading), (**b**) D_0, (**c**) logN_w, and (**d**) μ as measured by disdrometer 005 on 4 March 2019 from 0320 to 1100 UTC. Projection of each 1 min DSD in the (**e**) logN_w-D_0 and (**f**) LWC-D_0 parameter spaces. PPI of Z_H measured by the PAR radar at (**g**) 0330 UTC and (**h**) 0830 UTC. The marker color in (**a**–**f**) indicates the group according to the D18 classification. Dashed lines in (**a**–**d**) mark the times of the radar images. The rings in (**g**,**h**) indicate the 60, 120, and 180 km ranges. The white marker shows the position of the disdrometer.

After the initial convective phase, a transition period followed during which R decreased significantly, as well as D_0. LogN_w remained approximately constant, and μ increased significantly. Most of those data points were classified as ambiguous and some as Group 4 (stratiform), although there was no bright band signature observed yet.

The stratiform phase took place later, as observed by the PAR radar at 0830 UTC. The PPI in Figure 10h shows a widely spread system with uniform horizontal characteristics and moderate reflectivities of around 30 dBZ above the disdrometer. Figure 10a–d shows a stabilization of R and all other parameters. D_0 oscillated between 2 and 2.5 mm, exceeding 3 mm in some extreme cases. LogN_w oscillated around 2.5, and μ oscillated around two, adopting slightly smaller values than during the stratiform phase in Case 1, which was consistent with the much wider size spectrums (shading in Figure 10a). Data points during this final phase were classified as Group 4 (intense stratiform) and Group 6 (intense ice-based convection). Although Group 6 was mostly related to convective processes, it might also be associated with very intense stratiform precipitation (D18), which was clearly the case. Most data points in this final phase fell in the stratiform area of the BR09 separation, but some of the points classified as Group 6 crossed the separation, falling in the convective zone. That is why, in this case, the D18 classification worked better than BR09, since the latter would classify as convective some DSDs that were stratiform without doubt.

4. Discussion

The variability of the different DSD parameters was analyzed as a function of the distance to the SDC. Region A, which was the closest to the SDC, presented the highest number concentrations, smallest mean and maximum diameters, higher values of μ, and low R and LWC, while Region C, which was the farthest to the east of the SDC, exhibited much lower values of N_w, significantly larger D_0, D_m, and D_{max}, i.e., higher concentrations of bigger drops also denoted by lower values of μ, and, consequently, the largest values of LWC and R. Region B, located in the middle between A and C, presented intermediate characteristics. This suggests that the number of drops per unit volume decreased with the distance to the east of the SDC, while the mean size of drops increased, leading to an increase in LWC and R.

Then, the data were projected onto the D18 world EOFs and classified accordingly into Groups 1 to 6. Sixty-four percent of the data were below the imposed thresholds, falling into the "Ambiguous" category. The most frequent Groups were 4 (18%) and 6 (9%), related to intense stratiform rain associated with aggregation and riming processes and intense ice-based convection, respectively. Six percent of the data were classified as Group 2 (stratiform rain associated mainly with vapor deposition processes), and four percent were classified as Group 1 (convection). No data points were classified as Group 3 or Group 5. The latter was expected, since this category was almost non-existent in the mid-latitude dataset in D18 and is found mainly in the low latitudes. The lack of points classified as Group 3, however, might be due to the underrepresentation in the D18 world dataset of mountainous regions, subtropical latitudes, and the Southern Hemisphere. It might also be related to the lower values of N_w and the larger D_0 of the RELAMPAGO-CACTI dataset compared to the mid-latitude dataset in D18, which might also explain the fact that most non-ambiguous data points were classified as Group 4 and Group 6 and very few as Group 2 and Group 1.

Two distinct modes of variability were identified in Region A: at night, the DSD presented lower N_w and larger D_0, while in the afternoon, N_w increased and D_0 decreased. The elevated number concentrations and smaller mean diameters were compatible with orographic DSDs described in previous literature [17,18], and since this mode of variability was more frequent in the afternoon, it might be related to diurnal heating on the hillsides as a forcing mechanism of convection.

Finally, three case studies were presented. The first two were representative of Region A, one of the night regime (Case 1) and the other one of the afternoon regime (Case 2). The third one was representative of Region C. The aim was to relate the DSD characteristics

with the type of precipitation and microphysical processes involved, with the support of radar observations, in the context of the analysis proposed in D18. In Cases 1 and 3, the D18 classification worked fine, with most convective times being classified as Group 6 (intense ice-based convection) and some as Group 1 (convection), most stratiform data points being classified as Group 4 (intense stratiform), and some as Group 6, especially in Case 3 (Region C), where drops were bigger and N_w was lower, which might be related to large melted ice particles. In Case 2, however, most points fell into the "Ambiguous" category, and a few were classified as Group 2 and Group 4. Case 2 was an example of weak shallow convection in the afternoon in Region A, with N_w higher than in the other cases and smaller D_0. Radar observations suggested Case 2 was compatible with Group 3 in the D18 classification, although here, $\log N_w$ was significantly lower, which was why most data points fell in the "Ambiguous" category rather than being classified as Group 3. Again, the misclassification in this case might be explained by the differences between the D18 world dataset and the RELAMPAGO-CACTI dataset, as well as the underrepresentation of the study region in the former.

5. Conclusions

We presented a robust characterization of the DSD in Central Argentina based on the large amount of data collected during RELAMPAGO-CACTI, dividing the study region into three subregions in order to assess the impact of the proximity to the complex terrain of the Sierras de Córdoba (SDC).

The variability of the different DSD parameters was analyzed as a function of the distance to the SDC. The distribution of the different parameters suggested that the number of drops per unit volume decreased with the distance to the east of the SDC, while the mean size of drops increased, leading to an increase in LWC and R.

Furthermore, the disdrometers located closer to the SDC presented a bimodal distribution of D_0: the larger D_0 were associated with lower $\log N_w$ and occurred more frequently during the night, while the smaller D_0 were associated with higher values of $\log N_w$, compatible with orographic DSDs, and were found more frequently during the afternoon.

The data were classified following the methodology proposed in Dolan et al. (2018) (D18). The most frequent categories were those related to intense stratiform and intense convection, both associated with ice-based processes; fewer data points were classified as convective and stratiform alone, and no data points were classified as weak convection or convection associated with warm rain processes. The latter was expected, since that mode of variability of the DSD was found mainly at low latitudes. However, the lack of points classified as weak convection (small D_0 and high $\log N_w$), as well as the high frequency of intense stratiform (low $\log N_0$ and moderate D_0) and intense convection (low $\log N_w$ and large D_0) might be explained by the larger D_0 and lower $\log N_w$ of the RELAMPAGO-CACTI dataset compared to the global dataset analyzed in the cited article.

Finally, three case studies were analyzed. The first two corresponded to the two regimes observed in the region closest to the SDC: Case 1 corresponded to the night regime and Case 2 to the afternoon regime. Case 3 was representative of the easternmost region. The events were described with the aid of coincident radar observations. Case 1 and Case 3 consisted of an initial convective phase followed by a stratiform period, which was reflected on the temporal evolution of the DSD parameters, as well as the radar images, and the classification proposed in D18 worked well in both cases. However, Bringi et al.'s (2009) (BR09) separation misclassified some of the stratiform points in Case 3 mainly because of the larger D_0, characteristic of the study region and associated with the presence of big melted ice particles. Neither the D18 classification, nor the BR09 separation were able to correctly classify the data in Case 2, which consisted of weak shallow convection. According to the D18 classification, most data points were ambiguous, and the BR09 separation classified most data points as stratiform, when the DSD parameters and radar images indicated that it was a convective event.

Author Contributions: Conceptualization, C.C., P.S., and V.G.; methodology, C.C., P.S., V.G., and B.D.; software, C.C. and B.D.; writing—original draft preparation, C.C., P.S., and V.G.; writing—review and editing, C.C., P.S., V.G., B.D., and S.W.N. All authors read and agreed to the published version of the manuscript.

Funding: C.C. was supported by the Universidad de Buenos Aires student scholarship. The present work was supported by the projects from Argentina ANPCyT PICT 2017-0221 and PICT 2016-0710, UBACyT 20020130100618BA, the International cooperation project from Argentina, and CONICET—NSF 2356/18. S.W.N. would like to acknowledge support by the National Science Foundation (Grant AGS-1661799) and the Department of Energy Atmospheric Systems Research Subcontract 408988 from Pacific Northwest National Laboratory.

Data Availability Statement: Publicly available datasets were analyzed in this study. They can be found in the links provided in Section 2.

Acknowledgments: RMA1 and FDC data were provided by Secretaría de Infraestructura y Política Hídrica, Ministerio del Interior, Obras Públicas y Vivienda of the Argentinean National Government framed within the SINARAME Project. The National System of Weather Radars (Sistema Nacional de Radares Meteorológicos, SINARAME) project is an Argentinean effort to expand the radar network over the whole country. We acknowledge Walter Petersen for supporting the NASA GPM disdrometer deployment and Ali Tokay for performing quality control on these data. The RELAMPAGO disdrometers were supported by the National Science Foundation and the National Center for Atmospheric Research (NCAR) Earth Observing Laboratory and Research Applications Laboratory. We thank Francina Dominguez, David Gochis, Carlos Marcelo Garcia, and their teams for supporting the disdrometer deployment.

Conflicts of Interest: The authors declare no conflict of interest.

References

1. Chandrasekar, V.; Gorgucci, E.; Scarchilli, G. Optimization of Multiparameter Radar Estimates of Rainfall. *J. Appl. Meteorol. Climatol.* **1993**, *32*, 1288–1293. [CrossRef]
2. Rosenfeld, D.; Wolff, D.B.; Atlas, D. General Probability-matched Relations between Radar Reflectivity and Rain Rate. *J. Appl. Meteorol.* **1993**, *32*, 50–72. [CrossRef]
3. Giangrande, S.E.; Ryzhkov, A.V. Estimation of Rainfall Based on the Results of Polarimetric Echo Classification. *J. Appl. Meteorol. Climatol.* **2008**, *47*, 2445–2462. [CrossRef]
4. You, C.H.; Kang, M.Y.; Lee, D.I.; Uyeda, H. Rainfall estimation by S-band polarimetric radar in Korea. Part I: Preprocessing and preliminary results. *Meteorol. Appl.* **2014**, *21*, 975–983. [CrossRef]
5. Meyers, M.P.; Walko, R.L.; Harrington, J.Y.; Cotton, W.R. New RAMS cloud microphysics parameterization. Part II: The two-moment scheme. *Atmos. Res.* **1997**, *45*, 3–39. [CrossRef]
6. Saleeby, S.M.; Cotton, W.R. A Large-Droplet Mode and Prognostic Number Concentration of Cloud Droplets in the Colorado State University Regional Atmospheric Modeling System (RAMS). Part I: Module Descriptions and Supercell Test Simulations. *J. Appl. Meteorol.* **2004**, *43*, 182–195. [CrossRef]
7. Milbrandt, J.A.; Yau, M.K. A Multimoment Bulk Microphysics Parameterization. Part I: Analysis of the Role of the Spectral Shape Parameter. *J. Atmos. Sci.* **2005**, *62*, 3051–3064. [CrossRef]
8. Rosenfeld, D.; Ulbrich, C.W. Cloud Microphysical Properties, Processes, and Rainfall Estimation Opportunities. In *Radar and Atmospheric Science: A Collection of Essays in Honor of David Atlas*; Wakimoto, R.M., Srivastava, R., Eds.; American Meteorological Society: Boston, MA, USA, 2003; pp. 237–258. [CrossRef]
9. Bringi, V.N.; Chandrasekar, V.; Hubbert, J.; Gorgucci, E.; Randeu, W.L.; Schoenhuber, M. Raindrop Size Distribution in Different Climatic Regimes from Disdrometer and Dual-Polarized Radar Analysis. *J. Atmos. Sci.* **2003**, *60*, 354–365. [CrossRef]
10. Bringi, V.N.; Williams, C.R.; Thurai, M.; May, P.T. Using Dual-Polarized Radar and Dual-Frequency Profiler for DSD Characterization: A Case Study from Darwin, Australia. *J. Atmos. Ocean. Technol.* **2009**, *26*, 2107–2122. [CrossRef]
11. Thompson, E.J.; Rutledge, S.A.; Dolan, B.; Thurai, M. Drop Size Distributions and Radar Observations of Convective and Stratiform Rain over the Equatorial Indian and West Pacific Oceans. *J. Atmos. Sci.* **2015**, *72*, 4091–4125. [CrossRef]
12. Dolan, B.; Fuchs, B.; Rutledge, S.A.; Barnes, E.A.; Thompson, E.J. Primary Modes of Global Drop Size Distributions. *J. Atmos. Sci.* **2018**, *75*, 1453–1476. [CrossRef]
13. Ulbrich, C.W.; Atlas, D. Microphysics of Raindrop Size Spectra: Tropical Continental and Maritime Storms. *J. Appl. Meteorol. Climatol.* **2007**, *46*, 1777–1791. [CrossRef]
14. Thurai, M.; Bringi, V.N.; May, P.T. CPOL Radar-Derived Drop Size Distribution Statistics of Stratiform and Convective Rain for Two Regimes in Darwin, Australia. *J. Atmos. Ocean. Technol.* **2010**, *27*, 932–942. [CrossRef]
15. Jaffrain, J.; Berne, A. Experimental Quantification of the Sampling Uncertainty Associated with Measurements from PARSIVEL Disdrometers. *J. Hydrometeorol.* **2011**, *12*, 352–370. [CrossRef]

16. Friedrich, K.; Higgins, S.; Masters, F.J.; Lopez, C.R. Articulating and Stationary PARSIVEL Disdrometer Measurements in Conditions with Strong Winds and Heavy Rainfall. *J. Atmos. Ocean. Technol.* **2013**, *30*, 2063–2080. [CrossRef]
17. Zwiebel, J.; Van Baelen, J.; Anquetin, S.; Pointin, Y.; Boudevillain, B. Impacts of orography and rain intensity on rainfall structure. The case of the HyMeX IOP7a event. *Q. J. R. Meteorol. Soc.* **2016**, *142*, 310–319. [CrossRef]
18. Murata, F.; Terao, T.; Chakravarty, K.; Syiemlieh, H.J.; Cajee, L. Characteristics of Orographic Rain Drop-Size Distribution at Cherrapunji, Northeast India. *Atmosphere* **2020**, *11*. [CrossRef]
19. Zhang, H.; Zhang, Y.; He, H.; Xie, Y.; Zeng, Q. Comparison of Raindrop Size Distributions in a Midlatitude Continental Squall Line during Different Stages as Measured by Parsivel over East China. *J. Appl. Meteorol. Climatol.* **2017**, *56*, 2097–2111. [CrossRef]
20. Wen, J.; Zhao, K.; Huang, H.; Zhou, B.; Yang, Z.; Chen, G.; Wang, M.; Wen, L.; Dai, H.; Xu, L.; Liu, S.; Zhang, G.; Lee, W.C. Evolution of microphysical structure of a subtropical squall line observed by a polarimetric radar and a disdrometer during OPACC in Eastern China. *J. Geophys. Res. Atmos.* **2017**, *122*, 8033–8050. [CrossRef]
21. Chen, B.; Yang, J.; Pu, J. Statistical Characteristics of Raindrop Size Distribution in the Meiyu Season Observed in Eastern China. *J. Meteorol. Soc. Jpn. Ser.* **2013**, *91*, 215–227. [CrossRef]
22. Zipser, E.J.; Cecil, D.J.; Liu, C.; Nesbitt, S.W.; Yorty, D.P. Where Are the Most Intense Thunderstorms on Earth? *Bull. Am. Meteorol. Soc.* **2006**, *87*, 1057–1072. [CrossRef]
23. Mezher, R.N.; Doyle, M.; Barros, V. Climatology of hail in Argentina. *Atmos. Res.* **2012**, *114–115*, 70–82. [CrossRef]
24. Matsudo, C.; Salio, P. Severe weather reports and proximity to deep convection over Northern Argentina. *Atmos. Res.* **2011**, *100*, 523–537 . [CrossRef]
25. Rasmussen, K.L.; Zuluaga, M.D.; Houze, R.A., Jr. Severe convection and lightning in subtropical South America. *Geophys. Res. Lett.* **2014**, *41*, 7359–7366. [CrossRef]
26. Kumjian, M.R.; Gutierrez, R.; Soderholm, J.S.; Nesbitt, S.W.; Maldonado, P.; Luna, L.M.; Marquis, J.; Bowley, K.A.; Imaz, M.A.; Salio, P. Gargantuan Hail in Argentina. *Bull. Am. Meteorol. Soc.* **2020**, *101*, E1241–E1258. [CrossRef]
27. Albrecht, R.I.; Goodman, S.J.; Buechler, D.E.; Blakeslee, R.J.; Christian, H.J. Where Are the Lightning Hotspots on Earth? *Bull. Am. Meteorol. Soc.* **2016**, *97*, 2051–2068. [CrossRef]
28. Peterson, M.J.; Lang, T.J.; Bruning, E.C.; Albrecht, R.; Blakeslee, R.J.; Lyons, W.A.; Pédeboy, S.; Rison, W.; Zhang, Y.; Brunet, M.; et al. New World Meteorological Organization Certified Megaflash Lightning Extremes for Flash Distance (709 km) and Duration (16.73 s) Recorded From Space. *Geophys. Res. Lett.* **2020**, *47*, e2020GL088888. [CrossRef]
29. Altinger de Schwarzkopf, M.L.; Rosso, L.C. Severe Storms and Tornadoes in Argentina. In Proceedings of the 12th Conference on Severe Local Storms, American Meteorological Society, San Antonio, TX, USA, 12–15 January 1982 .
30. Dias, M.A.F.S. An Increase in the Number of Tornado Reports in Brazil. *Weather. Clim. Soc.* **2011**, *3*, 209–217. [CrossRef]
31. Mulholland, J.P.; Nesbitt, S.W.; Trapp, R.J.; Rasmussen, K.L.; Salio, P.V. Convective Storm Life Cycle and Environments near the Sierras de Córdoba, Argentina. *Mon. Weather. Rev.* **2018**, *146*, 2541–2557. [CrossRef]
32. Cancelada, M.; Salio, P.; Vila, D.; Nesbitt, S.W.; Vidal, L. Backward Adaptive Brightness Temperature Threshold Technique (BAB3T): A Methodology to Determine Extreme Convective Initiation Regions Using Satellite Infrared Imagery. *Remote. Sens.* **2020**, *12*, 337. [CrossRef]
33. Nesbitt, S.W.; Salio, P.V.; Ávila, E.; Bitzer, P.; Carey, L.; Chandrasekar, V.; Deierling, W.; Dominguez, F.; Dillon, M.E.; Garcia, C.M.; et al. A storm safari in Subtropical South America: Proyecto RELAMPAGO. *Bull. Am. Meteorol. Soc.* **2021**, 1–64. [CrossRef]
34. Varble, A.C.; Nesbitt, S.W.; Salio, P.; Hardin, J.C.; Bharadwaj, N.; Borque, P.; DeMott, P.J.; Feng, Z.; Hill, T.C.J.; Marquis, J.N.; et al. Utilizing a Storm-Generating Hotspot to Study Convective Cloud Transitions: The CACTI Experiment. *Bull. Am. Meteorol. Soc.* **2021**, 1–67. [CrossRef]
35. Löffler-Mang, M.; Joss, J. An Optical Disdrometer for Measuring Size and Velocity of Hydrometeors. *J. Atmos. Ocean. Technol.* **2000**, *17*, 130–139. [CrossRef]
36. Löffler-Mang, M.; Blahak, U. Estimation of the Equivalent Radar Reflectivity Factor from Measured Snow Size Spectra. *J. Appl. Meteorol.* **2001**, *40*, 843–849. [CrossRef]
37. Tokay, A.; Wolff, D.B.; Petersen, W.A. Evaluation of the New Version of the Laser-Optical Disdrometer, OTT Parsivel^2. *J. Atmos. Ocean. Technol.* **2014**, *31*, 1276–1288. [CrossRef]
38. Yuter, S.E.; Kingsmill, D.E.; Nance, L.B.; Löffler-Mang, M. Observations of Precipitation Size and Fall Speed Characteristics within Coexisting Rain and Wet Snow. *J. Appl. Meteorol. Climatol.* **2006**, *45*, 1450–1464. [CrossRef]
39. Tokay, A.; Kruger, A.; Krajewski, W.F. Comparison of Drop Size Distribution Measurements by Impact and Optical Disdrometers. *J. Appl. Meteorol.* **2001**, *40*, 2083–2097. [CrossRef]
40. Kruger, A.; Krajewski, W.F. Two-Dimensional Video Disdrometer: A Description. *J. Atmos. Ocean. Technol.* **2002**, *19*, 602–617. [CrossRef]
41. Thurai, M.; Bringi, V.N. Drop Axis Ratios from a 2D Video Disdrometer. *J. Atmos. Ocean. Technol.* **2005**, *22*, 966–978. [CrossRef]
42. Tokay, A.; Petersen, W.A.; Gatlin, P.; Wingo, M. Comparison of Raindrop Size Distribution Measurements by Collocated Disdrometers. *J. Atmos. Ocean. Technol.* **2013**, *30*, 1672–1690. [CrossRef]
43. Gunn, R.; Kinzer, G.D. The Terminal Velocity of Fall for Water Droplets in Stagnant Air. *J. Meteorol.* **1949**, *6*, 243–248. [CrossRef]
44. Foote, G.B.; Toit, P.S.D. Terminal Velocity of Raindrops Aloft. *J. Appl. Meteorol. Climatol.* **1969**, *8*, 249–253. [CrossRef]
45. Smith, P.L.; Liu, Z.; Joss, J. A Study of Sampling-Variability Effects in Raindrop Size Observations. *J. Appl. Meteorol.* **1993**, *32*, 1259–1269. [CrossRef]

46. Smith, P.L. Sampling Issues in Estimating Radar Variables from Disdrometer Data. *J. Atmos. Ocean. Technol.* **2016**, *33*, 2305–2313. [CrossRef]
47. Petty, G.W.; Huang, W. The Modified Gamma Size Distribution Applied to Inhomogeneous and Nonspherical Particles: Key Relationships and Conversions. *J. Atmos. Sci.* **2011**, *68*, 1460–1473. [CrossRef]
48. Marshall, J.S.; Palmer, W.M.K. The Distribution of Raindrops with Size. *J. Meteorol.* **1948**, *5*, 165–166. [CrossRef]
49. Junge, C.E.; Robinson, E.; Ludwig, F.L. A Study of Aerosols in Pacific Air Masses. *J. Appl. Meteorol.* **1969**, *8*, 340–347. [CrossRef]
50. Ulbrich, C.W. Natural Variations in the Analytical Form of the Raindrop Size Distribution. *J. Clim. Appl. Meteorol.* **1983**, *22*, 1764–1775. [CrossRef]
51. Willis, P.T. Functional Fits to Some Observed Drop Size Distributions and Parameterization of Rain. *J. Atmos. Sci.* **1984**, *41*, 1648–1661. [CrossRef]
52. Testud, J.; Oury, S.; Black, R.A.; Amayenc, P.; Dou, X. The Concept of "Normalized" Distribution to Describe Raindrop Spectra: A Tool for Cloud Physics and Cloud Remote Sensing. *J. Appl. Meteorol.* **2001**, *40*, 1118–1140. [CrossRef]
53. Hardin, J.; Guy, N. Available online: https://zenodo.org/record/9991 (accessed on 1 October 2019).
54. Thurai, M.; Gatlin, P.; Bringi, V.N.; Petersen, W.; Kennedy, P.; Notaroš, B.; Carey, L. Toward Completing the Raindrop Size Spectrum: Case Studies Involving 2D-Video Disdrometer, Droplet Spectrometer, and Polarimetric Radar Measurements. *J. Appl. Meteorol. Climatol.* **2017**, *56*, 877–896. [CrossRef]
55. Giangrande, S.E.; Luke, E.P.; Kollias, P. Characterization of Vertical Velocity and Drop Size Distribution Parameters in Widespread Precipitation at ARM Facilities. *J. Appl. Meteorol. Climatol.* **2012**, *51*, 380–391. [CrossRef]
56. Saulo, A.; Nicolini, M.; Chou, S. Model characterization of the South American low-level flow during the 1997–1998 spring–summer season. *Clim. Dyn.* **2000**, *16*, 867–881. [CrossRef]
57. Nicolini, M.; Saulo, A.; Torres, J.; Salio, P. Enhanced precipitation over Southeastern South America related to strong low-level jet events during austral warm season. *Meteorol. Spec. Issue S. Am. Monsoon Syst.* **2002**, *27*, 59–69.
58. Salio, P.; Nicolini, M.; Zipser, E.J. Mesoscale Convective Systems over Southeastern South America and Their Relationship with the South American Low-Level Jet. *Mon. Weather. Rev.* **2007**, *135*, 1290–1309. [CrossRef]
59. Helmus, J.; Collis, S. The Python ARM Radar Toolkit (Py-ART), a Library for Working with Weather Radar Data in the Python Programming Language. *J. Open Res. Softw.* **2016**. [CrossRef]